NISTIR 7283

APEX Blind Deconvolution of Real Hubble Space Telescope Imagery and Other Astronomical Data

Carasso, Alfred S.

National Institute of Standards and Technology
U.S. Department of Commerce

NISTIR 7283

APEX Blind Deconvolution of Real Hubble Space Telescope Imagery and Other Astronomical Data

Carasso, Alfred S.
Mathematical and Computational Sciences Division
National Institute of Standards and Technology
Gaithersburg, MD 20899

December 2005

U.S. Department of Commerce
Carlos M. Gutierrez, Secretary

Technology Administration
Michelle O'Neill, Acting Under Secretary of Commerce for Technology

National Institute of Standards and Technology
William Jeffrey, Director

APEX BLIND DECONVOLUTION OF REAL HUBBLE SPACE TELESCOPE IMAGERY AND OTHER ASTRONOMICAL DATA

ALFRED S. CARASSO*

Abstract. The APEX method is a non-iterative, single frame, direct blind deconvolution technique that can sharpen certain kinds of high resolution images in quasi real-time. The method is predicated on a restricted class of blurs, in the form of 2D heavy-tailed bell-shaped surfaces. Not all images can be usefully enhanced with the APEX method. Nevertheless, the method is found effective on a broad class of galaxy images, including *color* Hubble Space Telescope ACS imagery. APEX-detected optical transfer functions that successfully sharpen these images are far from Gaussian, and of a type not commonly found in the astronomical imaging literature. Visually striking enhancements are obtained, with significant sharpening confirmed by better than threefold increases in image gradient norms.

1. Introduction. The APEX method is a non-iterative, single frame, direct blind deconvolution technique that can sharpen certain kinds of high resolution images in quasi real-time. The method operates in Fourier transform space via FFT algorithms. Typically, 1024×1024 pixel images can be processed in seconds on current desktop computers. The method has been applied successfully in diverse imaging contexts, including airborne reconnaissance, MRI and PET brain scans, and scanning electron microscopy [4, 5, 6]. However, not all images can be usefully enhanced with the APEX method. The present paper explores the possible application of this technique to astronomical data, including Hubble Space Telescope (HST) imagery. In Figure 1, a familiar earthbound setting illustrates the type of improvement that is sometimes possible with the APEX method. In that example, zooming on selected parts of the APEX-enhanced image 1(B) reveals buildings in the distance, Holstein cows grazing in the meadow, and numerous other fine-scale details not readily apparent in the original image 1(A). See [5].

In recent years, much excellent work has been done in the area of blind deconvolution of astronomical data. See e.g., [1], [10], [13], [19], [23], [24], [29], and [30]. Many of these methods aim primarily at undoing the distorting effects of atmospheric turbulence in short-exposure, ground-based observations. Multiframe algorithms, typically involving several hundred short-exposure images of the same object, appear to be particularly effective. An interesting example of multiframe blind deconvolution, in the context of ground-based surveillance of space objects, is given in [24].

APEX processing is typically not useful in such short-exposure applications, and the method would probably be incapable of reproducing the results in [24]. In a similar vein, consider the severely blurred early Hubble Space Telescope imagery caused by manufacturing flaws in the primary mirror. The much improved imagery following the 1993 implementation of corrective optics is best illustrated with the M100 galaxy images in Figure 2. Here, if APEX processing were to be applied to the single frame blurred image in Figure 2(A), the method would be unable to identify the flawed optics point spread function from the data in 2(A), and it would fail to produce a useful approximation to the sharp image in Figure 2(B).

The APEX method is predicated on an important but circumscribed class of radially symmetric shift-invariant blurs, one that generalizes Gaussian and Lorentzian distributions. This is the class **G** defined in Eq. (4) below. That class does not include

*Mathematical and Computational Sciences Division, National Institute of Standards and Technology, Gaithersburg, MD 20899. (alfred.carasso@nist.gov).

A **B**

Fig. 1. *APEX blind deconvolution of English village image. (A) Original* 512×512 *8-bit image. (B) APEX processed image. Zooming on selected parts of sharpened image (B) reveals buildings in the distance, and other significant information not easily detectable in image (A). See [5].*

A **B**

Fig. 2. *Hubble Space Telescope image of M100 galaxy, before and after implementation of corrective optics package. APEX method applied to image (A) would be unable to detect flawed optics psf, and would fail to produce useful approximation to image (B).*

the more complex point spread functions that characterize the examples mentioned in the preceding paragraph. Rather, the APEX method aims primarily at reconstructing fine scale information that may have been smoothed out by the combined effects of radially symmetric lens aberrations, long-exposure turbulence if present, and additional radially symmetric blurring, originating from diverse electron optical devices used in the acquisition and recording of the final digitized image. Presumably, the

APEX method will be successful on a given image, only to the extent that a significant portion of the unknown image blur can be well-approximated by some member of the class **G**.

It develops that APEX processing is surprisingly effective on a broad class of galaxy images, including *color* Hubble Space Telescope imagery. The APEX-detected optical transfer functions that successfully sharpen these images are very far from Gaussian, and of a type not commonly found in the astronomical imaging literature. Some visually striking enhancements are exhibited in sections 8 and 9. Sharpening in these images can be quantitatively assessed by evaluating image gradient norms, and threefold increases in gradient norms are commonly realized. Remarkably, for Hubble imagery, the APEX method can enhance Advanced Camera for Surveys (ACS) images, in addition to Wide Field Planetary Camera 2 (WFPC2) images. An interesting new method of assessing image sharpness, based on measuring image *Lipschitz exponents* [7], can be fruitfully applied to the present class of images. However, due to space limitations, a full discussion of this technique must be postponed to a future report.

2. Heavy-tailed Lévy point spread functions. Important empirical work [14], [15], has identified the general functional form of the optical transfer functions (otf) in a very wide variety of electron optical imaging devices, including phosphor screens, and some types of photographic film. Define the 2D Fourier transform of any function $h(x, y)$ by

$$\hat{h}(\xi,\eta) \equiv \int_{R^2} h(x,y) exp\{-2\pi i(\xi x+\eta y)\} dx dy. \tag{1}$$

When $h(x, y)$ is a point spread function (psf), it is non-negative and integrates to unity. Such a function corresponds to a probability density function. The optical transfer function $\hat{h}(\xi, \eta)$ corresponds to the characteristic function of that density. According to [14], [15], most electronic imaging devices have otfs that can be expressed by

$$\hat{h}(\xi,\eta) = exp\{-\alpha(\xi^2+\eta^2)^\beta\}, \qquad \alpha > 0, \quad 0 < \beta \le 1. \tag{2}$$

where the constants α and β depend on the particular device. The corresponding densities $h(x, y)$ are bell-shaped surfaces in physical $x,\ y$ space, and belong to the class of radially symmetric Lévy stable laws, [9], [20]. The constant $\alpha > 0$ in Eq. (2) controls the width of the density $h(x, y)$, and $h(x, y)$ approaches the Dirac δ-function as $\alpha \to 0$. The constant β is called the Lévy exponent. The case $\beta = 1$ in Eq. (2) corresponds to the Gaussian distribution, while the case $\beta = 1/2$ corresponds to the 2D Lorentzian density

$$h(x,y) = \frac{\alpha}{2\pi(x^2+y^2+\alpha^2)^{3/2}}, \qquad (x,y) \in R^2. \tag{3}$$

For other values of $\beta,\ 0 < \beta \le 1$, in Eq. (2), the corresponding density $h(x, y)$ is not known in closed form in the physical variables $x,\ y$. In the Gaussian case $\beta = 1$, $h(x, y)$ has exponentially decaying slim tails and finite variance. However, for $0 < \beta < 1$, $h(x, y)$ has infinite variance, with heavy tails that decay like a power of $1/r$, where $r = (x^2 + y^2)^{1/2}$. See [2], [9], [20], [22], [32].

The expression in Eq. (2) can be used to describe other important types of blurs. As shown in [12], the otf for long-exposure turbulence blurring is given by Eq. (2) with $\beta = 5/6$ and α determined by atmospheric conditions. In [16], it is shown that the analytically known diffraction-limited otf for a perfect lens can be approximated over a wide frequency range by Eq. (2), with $\beta = 3/4$ and α a properly chosen function of the cutoff frequency. In [17], otf data for 56 different kinds of photographic film are analyzed. Good agreement is found when these data are fitted with Eq. (2), and the pairs (α, β) characterizing each of these 56 otfs are identified. It is found that 36 types of film have otfs where $1/2 \leq \beta \leq 1$. The remaining 20 types have values of β in the range $0.265 \leq \beta \leq 0.475$. Corresponding psfs are very far from Gaussian.

3. Generalized Central Limit Theorem and the APEX method. The classical Central Limit Theorem considers the limiting probability distribution of normalized sums of large numbers of independent random variables with *finite variance*, and it asserts that that limit is always a Gaussian distribution [9]. In fact, Gaussians are often used to fit empirically obtained bell-shaped data, and this choice is usually justified on the basis of that theorem. For an example of just such an approach applied to electron optics point spread functions, see [31].

In recent years, with the advent of more sophisticated measurement methods, numerous physical situations have been uncovered where Gaussians provide inadequate descriptions of observed bell-shaped data, because legitimate heavy-tailed behavior cannot be accomodated, [2], [25], [32]. A recent example from high energy particle physics, leading to an instructive discussion of the need to consider non-Gaussian distributions, is given in [8]. It is now generally recognized that such heavy-tailed data reflect underlying random processes with *infinite variance*, and that such processes are pervasive in nature [28]. The empirical work reported in [14], [15], [17], is simply one instance of a recurring pattern.

The Generalized Central Limit Theorem considers normalized sums of independent, identically distributed random variables, with variances that need not be finite. According to that theorem, the limit of any such sum, if it exists, must be a Lévy stable law, [9], [22]. Note that while the class of stable laws includes more complex asymmetric specimens, this paper restricts attention to the radially symmetric case through Eq. (2)

In some applications, several electron-optical devices may be cascaded together and used to image objects through a distorting medium such as the atmosphere. The overall psf is then the convolution product of the individual component psfs,

$$\hat{h}(\xi, \eta) = exp\{-\sum_{i=1}^{J} \alpha_i (\xi^2 + \eta^2)^{\beta_i}\}, \qquad \alpha_i \geq 0, \quad 0 < \beta_i \leq 1. \tag{4}$$

The general functional form given in Eq. (4) may also be used to best-fit a large class of empirically determined optical transfer functions, by suitable choices of the parameters α_i, β_i, and J.

We define the class **G** of blurring kernels to be the class of all psfs $h(x, y)$ whose Fourier transforms satisfy Eq. (4). We shall be interested in image deblurring problems

$$Hf \equiv \int_{R^2} h(x-u, y-v) f(u, v) du dv \equiv h(x, y) \otimes f(x, y) = g(x, y), \tag{5}$$

where $g(x, y)$ is the recorded blurred image, $f(x, y)$ is the desired unblurred image, and $h(x, y)$ is a known point spread function in class **G**. The blurred image $g(x, y)$ includes noise, which is viewed as a separate additional degradation,

$$g(x, y) = g_e(x, y) + n(x, y). \tag{6}$$

Here, $g_e(x,y)$ is the blurred image that would have been recorded in the absence of noise, and $n(x,y)$ represents the cumulative effects of all errors affecting final acquisition of the digitized array $g(x,y)$. The unique solution of Eq. (5) when the right hand side is $g_e(x,y)$, is the exact sharp image denoted by $f_e(x,y)$. Thus

$$h(x,y) \otimes f_e(x,y) = g_e(x,y). \tag{7}$$

With class **G** psfs we may define fractional powers $H^t,\ 0 \le t \le 1$, of the convolution integral operator H in Eq. (5) as follows

$$H^t f \equiv \mathcal{F}^{-1}\left\{\hat{h}^t(\xi,\eta)\hat{f}(\xi,\eta)\right\}, \qquad 0 \le t \le 1. \tag{8}$$

Class **G** psf's are intimately related to diffusion processes, in that $u(x,y,t) = H^t f$ is the solution at time t of a generalized diffusion equation, (see Eq. (13) below).

These considerations underlie the APEX blind deconvolution approach, which stipulates at the outset that the blurring is isoplanatic, and that the lumped total system optical transfer function can be well approximated by Eq. (4). The APEX method is based on detecting such Lévy stable psfs by appropriate Fourier analysis of the blurred image data. As discussed more fully below, detected representative values for the constants α_i and β_i in Eq. (4) are used to construct a candidate otf. This is then used in the SECB deconvolution method, implemented as a *time-reversed diffusion equation.* By marching backwards in time, one can visually monitor the deconvolution process as it unfolds, examine accompanying diagnostic information, and, if necessary, choose to terminate that process prior to completion. Early termination is equivalent to interactive readjustment of the initial candidate otf.

4. Images and their Fourier transforms. The Fourier transform is the primary computational tool used in this paper. We deal exclusively with square images $g(x,y)$ of size $2N \times 2N$ pixels. In order to render mathematical formulae more transparent, we use the same notation, $\hat{g}(\xi,\eta)$, for both discrete and continuous Fourier transforms. In the discrete FFT case, the frequencies ξ and η are understood to be integer-valued and to range from $-N$ to N. Likewise, $g(x,y)$ denotes both discrete and continuous images. In the discrete case, the variables $x,\ y$ are measured in pixels and range from 1 to $2N$.

Given the Lévy pairs $(\alpha_i,\beta_i),\ i = 1,J$, where $\alpha_i > 0,\ 0 < \beta_i \le 1$, the corresponding discrete class **G** otf is the $2N \times 2N$ array $\hat{h}(\xi,\eta)$ where, with integer ξ,η

$$\hat{h}(\xi,\eta) = exp\{-\sum_{i=1}^{J} \alpha_i(\xi^2+\eta^2)^{\beta_i}\}, \qquad -N < \xi,\eta \le N. \tag{9}$$

In this paper, typical parameter values might be $N = 512,\ J = 1,\ \alpha = 0.2,\ \beta = 0.2$. Such otf arrays are used to construct the SECB deblurred image, as in Eq. (14) below.

Given an image $g(x,y)$, the natural *logarithm* of the absolute value of its Fourier transform, ln $|\hat{g}(\xi,\eta)|$, will play a crucial role. This logarithm is well-defined except where $\hat{g}(\xi,\eta) = 0$. At any such zero, we simply redefine $\hat{g}$ to be the machine epsilon. In practice, exact zeroes of $\hat{g}(\xi,\eta)$ are seldom encountered due to system noise.

The qualitative behavior in Fourier space of a large class of astronomical images is of interest. Let $f_e(x,y)$ be an exact sharp image as in (7). Since $f_e(x,y) \ge 0$

$$|\hat{f}_e(\xi,\eta)| \le \int_{R^2} f_e(x,y)dxdy = \hat{f}_e(0,0) = \gamma > 0. \tag{10}$$

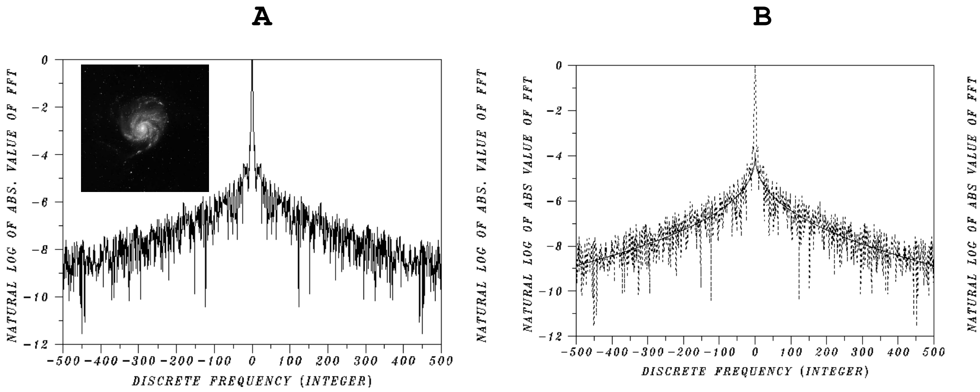

FIG. 3. *Fourier behavior in* 1024×1024 *image of spiral galaxy M101 is typical of a large class of astronomical images. Above image was taken by Jacoby, Bohannan and Hanna, Kitt Peak National Observatory, (NOAO/AURA/NSF). (A) ln* $|\hat{g}^*(\xi, 0)|$ *on* $|\xi| \leq 500$ *for M101 image. While local behavior is highly oscillatory, global behavior is generally monotone decreasing and convex. (B) Least squares fit of ln* $|\hat{g}^*(\xi, 0)|$ *with* $u(\xi) = -\alpha|\xi|^{2\beta} - A$*, with* $A = 3.85$*. Fit develops cusp at* $\xi = 0$ *and returns* $\alpha = 0.385, \beta = 0.206$*. Such trial least squares fits, using different values of* $A > 0$*, are basic to the APEX method.*

Also, since $g_e(x, y) = h(x, y) \otimes f_e(x, y)$ and $h(x, y)$ is a probability density,

$$\hat{g}_e(0,0) = \int_{R^2} g_e(x,y)dxdy = \int_{R^2} f_e(x,y)dxdy$$

$$= \hat{f}_e(0,0) = \gamma > 0. \tag{11}$$

Using γ as a normalizing constant, we may normalize any Fourier transform quantity $\hat{q}(\xi, \eta)$ by dividing by γ. Let

$$\hat{q}^*(\xi, \eta) = \hat{q}(\xi, \eta)/\gamma, \tag{12}$$

denote the normalized quantity. The function $|\hat{f}_e^{\,*}(\xi, \eta)|$ is highly oscillatory, and $0 \leq |\hat{f}_e^{\,*}| \leq 1$. Since $f_e(x, y)$ is real, its Fourier transform is conjugate symmetric. Therefore, the function $|\hat{f}_e^{\,*}(\xi, \eta)|$ is symmetric about the origin on any line through the origin in the (ξ, η) plane. The same is true for the blurred image data $|\hat{g}^*(\xi, \eta)|$.

For any $2N \times 2N$ image $g(x, y)$, the discrete FFT $\hat{g}(\xi, \eta)$ is a $2N \times 2N$ array of complex numbers. The frequencies ξ, η are integers lying between $-N$ and N, and the zero frequency is at the center of the transform array. This ordering is achieved by pre-multiplying $g(x, y)$ by $(-1)^{x+y}$. We shall be interested in the values of such transforms along single lines through the origin in the discrete (ξ, η) plane. The discrete transforms $|\hat{g}^*(\xi, 0)|$, and $|\hat{g}^*(0, \eta)|$ are immediately available. Image rotation may be used to obtain transforms along other directions. All 1-D Fourier plots shown in this paper are taken along the axis $\eta = 0$ in the (ξ, η) plane, as is the case in Figure 3. In these plots, the zero frequency is at the center of the horizontal axis, and the graphs are necessarily symmetric about the vertical line $\xi = 0$.

The class of astronomical images $g(x, y)$ considered in the present paper can be described in terms of the behavior of $\ln\ |\hat{g}^*(\xi, \eta)|$ along single lines through the origin in the (ξ, η) plane. While local behavior is highly oscillatory, global behavior is generally monotone decreasing and *convex* on $\xi \geq 0$. This is shown in Figure 3(A) for a typical galaxy image along the line $\eta = 0$, and similar behavior is found along other lines through the origin in the (ξ, η) plane. A least squares fit to the oscillatory trace in Figure 3(A) with a smooth curve, provides a good representation of this global monotone convexity property on $\xi \geq 0$. (A convex function is such that given any two distinct points A and B on its graph, the straight line segment joining A and B lies above the graph.) Many astronomical images exhibit similar globally monotone convex Fourier behavior. An example of an image where this is not the case, lies in the defective optics, blurred M100 image in Figure 2(A). In RGB color space, the red component of that image deviates strongly from convex monotone behavior. Use of the APEX method in the manner to be described below is intended only for images where Fourier behavior is similar to that shown in Figure 3(A).

5. SECB deblurring and diffusion equations. The SECB method is a direct (non-iterative) FFT-based image deblurring technique designed for equations in the form of Eq. (5), where $h(x, y)$ is assumed known and belongs to $\mathbf{G}$. A complete discussion of that method, together with error bounds and comparisons with other methods, may be found in [3]. Significantly, the SECB method does not impose smoothness requirements, such as prescribed bounds on the Laplacian or other derivatives of the unknown image $f(x, y)$. This is an important consideration since many images have sharp edges and other localized non-differentiable features. In addition, knowledge of the actual statistical character of the data noise $n(x, y)$ in Eq. (6) is not required, and the noise may be multiplicative. However, an estimate of the L^2 norm of $n(x, y)$ is required.

Considerable experience has been accumulated with the SECB method. That experience indicates that the SECB method can often recover fine-scale features in cases where this is not feasible with iterative methods such as the Lucy-Richardson, Maximum Entropy, or Marquina-Osher methods. Documented numerical experiments supporting these claims may be found in [3], [5], and [7].

Class $\mathbf{G}$ psfs are the Green's functions for certain linear fractional diffusion equations. As a consequence, the blurred noisy image $g(x, y)$ on the right of Eq. (5) can be interpreted as the noise corrupted solution, at time $t = 1$, of the diffusion initial value problem

$$\begin{aligned} \frac{\partial u}{\partial t} &= -\sum_{i=1}^{J} \lambda_i (-\Delta)^{\beta_i} u, \qquad 0 < t \leq 1. \\ u(x, y, 0) &= f_e(x, y), \end{aligned} \tag{13}$$

where $\lambda_i = \alpha_i (4\pi^2)^{-\beta_i}$, and Δ denotes the Laplacian. When the exact initial value $f_e(x, y)$ is given, $u(x, y, t) = H^t f_e$ is the solution of Eq. (13) at time t, and $u(x, y, 1) = g_e(x, y)$, in agreement with Eq. (7).

Solving the deconvolution problem in Eq. (5) is equivalent to solving the ill-posed *backwards in time* problem in Eq. (13), namely, given the noisy data $g(x, y)$ at time $t = 1$, find an approximation $f(x, y)$ to the initial data $f_e(x, y)$. The SECB method is a regularization method for solving that ill-posed diffusion problem, one that takes into account the presence of noise in the blurred image data $g(x, y)$ at $t = 1$. The SECB deblurred image $f^\dagger(x, y)$ is an approximation to $f_e(x, y)$ that is obtained in closed form in Fourier space. With $\overline{z}$ denoting the complex conjugate of z,

$$\hat{f}^\dagger(\xi, \eta) = \frac{\overline{\hat{h}}(\xi, \eta) \hat{g}(\xi, \eta)}{|\hat{h}(\xi, \eta)|^2 + K^{-2} |1 - \hat{h}^s(\xi, \eta)|^2}, \tag{14}$$

leading to $f^{\dagger}(x,y)$ upon inverse transforming. Here, the positive constants $s \ll 1$, and K, are regularization parameters, chosen on the basis of prior information as discussed in [5]. Typical values used in this paper might be $s = 0.01$, $K = 1000$. As in Eq. (8), we also form and display

$$u^{\dagger}(x,y,t) = H^t f^{\dagger}(x,y), \tag{15}$$

for selected *decreasing* values of t lying between 1 and 0. This simulates *marching backwards in time* in (13), and allows *monitoring* the gradual deblurring of the image. As $t \to 0$ the partial restorations $u^{\dagger}(x,y,t)$ become sharper. Such *slow motion* deconvolution allows detection of features in the image before they become obscured by noise or ringing artifacts. As will be seen below, such marching backwards in time is a vital element in the APEX method. Diagnostic statistical information about $u^{\dagger}(x,y,t)$ can also be calculated for selected values of t as $t \to 0$. Of particular interest are the discrete L^1 norm, defined as follows for $2N \times 2N$ images

$$\| u^{\dagger}(t) \|_{L^1} = (2N)^{-2} \sum_{x,y=1}^{2N} |u^{\dagger}(x,y,t)|, \tag{16}$$

and the discrete *total variation* or TV norm, which measures image gradients

$$\| u^{\dagger}(t) \|_{TV} = (2N)^{-2} \sum_{x,y=1}^{2N-1} \left(\{u_x^{\dagger}(x,y,t)\}^2 + \{u_y^{\dagger}(x,y,t)\}^2 \right)^{1/2}, \tag{17}$$

where

$$\begin{aligned} u_x^{\dagger}(x,y,t) &= (2N)^{-1}(u^{\dagger}(x+1,y,t) - u^{\dagger}(x,y,t)) \\ u_y^{\dagger}(x,y,t) &= (2N)^{-1}\left(u^{\dagger}(x,y+1,t) - u^{\dagger}(x,y,t)\right) \end{aligned} \tag{18}$$

In blind deconvolution applications of the SECB method, APEX-detected values for α_i, β_i, are used to form the $2N \times 2N$ array in Eq. (9). This is input into Eq. (14), and inverse FFT algorithms are then used to obtain $u^{\dagger}(x,y,t)$ in Eq. (15). This may result in individual pixel values that are negative. Accordingly, all negative values are reset to the value zero. For such non-negative image data, the discrete L^1 norm $\| u^{\dagger}(t) \|_{L^1}$ in Eq. (16) is proportional to the *total flux*. In a well-behaved deconvolution process, this total flux should be *conserved*, and $\| u^{\dagger}(t) \|_{L^1}$ should remain constant, as $t \to 0$. At the same time, the discrete image gradient norm $\| u^{\dagger}(t) \|_{TV}$ in Eq. (17) should *increase monotonically* as $t \to 0$, reflecting the gradual sharpening of edges and other localized singularities in the restored image.

6. A priori non-uniqueness in blind deconvolution. Blind deconvolution seeks to deblur an image without knowing the cause of the blur. This is a difficult mathematical problem in which severe ill-conditioning is compounded with non-uniqueness of solutions. A-priori constraints can reduce, but not entirely eliminate, the multiplicity of solutions. While many of these solutions are physically meaningless and can be rejected on physical grounds, there often remain infinitely many visually distinct, physically meaningful solutions. Consider the experiment in Figure 4.

The sharp 512×512 Sydney image $f_e(x,y)$ in Figure 4(A) was synthetically blurred by convolution with a Lorentzian density $h(x,y)$ with $\alpha_0 = 0.075$, $\beta_0 = 0.5$. This produced the blurred image $g_e(x,y)$ in Figure 4(B). To avoid distractions

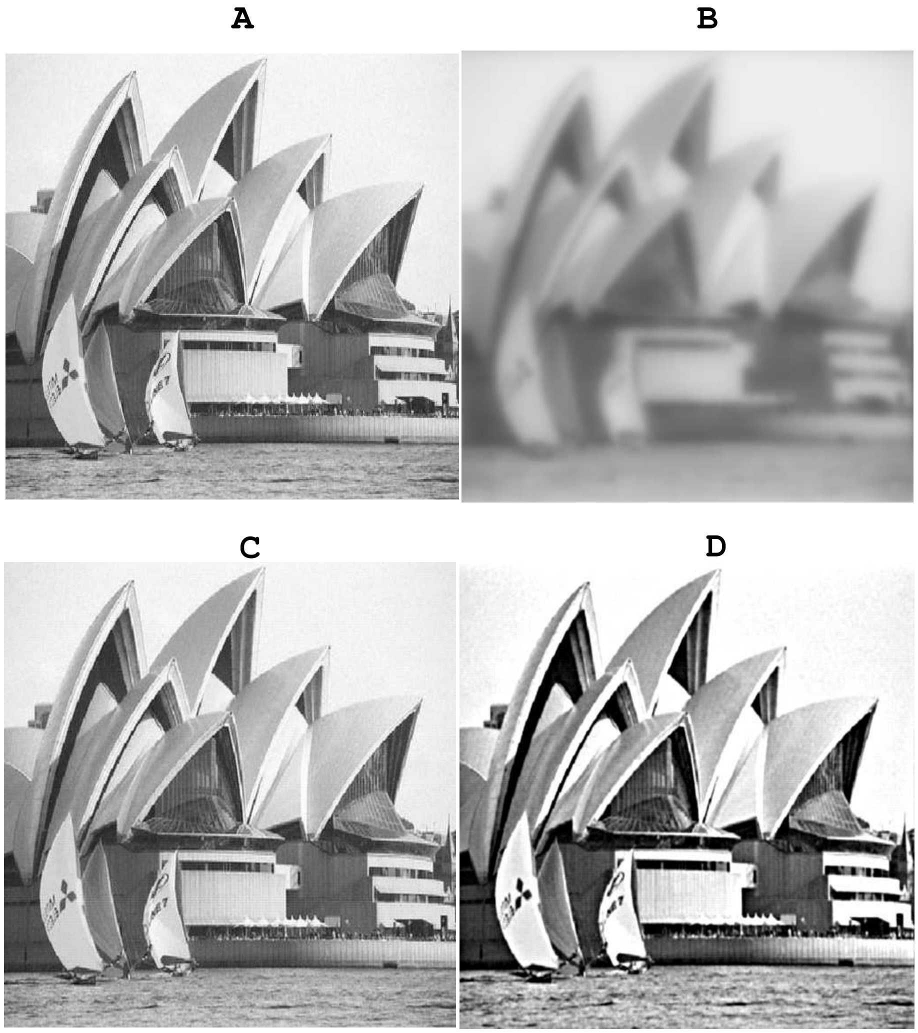

FIG. 4. *Non-uniqueness in blind deconvolution. Distinct point spread functions exist that produce distinct high quality reconstructions from the same blurred image. (A) Original sharp* 512×512 *Sydney image. (B) Synthetically blurred Sydney image created by convolution with Lorentzian density obtained by choosing* $\alpha = 0.075$, $\beta = 0.5$ *in Eq. (2). (C) Deblurring of image (B) using correct otf parameters* $\alpha = 0.075$, $\beta = 0.5$. *(D) Deblurring of image (B) using "incorrect" otf parameters* $\alpha = 0.195$, $\beta = 0.4$. *Deblurred images obtained using SECB procedure in Section 5, with* $s = 0.001$ *and* $K = 10000$.

caused by noise, the blurred image $g_e(x, y)$ in this experiment was computed and stored in 64-bit precision. Deblurring Figure 4(B) with the correct psf values $\alpha = 0.075$, $\beta = 0.5$, produces Figure 4(C). This is in excellent visual agreement with $f_e(x, y)$ in Figure 4(A), as expected. However, Figure 4(D), obtained from Figure 4(B) using the "incorrect" psf values $\alpha = 0.195, \beta = 0.4$, appears even sharper! It is not evident how, or *why*, one would eliminate the reconstruction in 4(D). Both deblurred images were obtained using the SECB method with $s = 0.001$ and $K = 10000$. One dimensional cross sections of the two distinct psfs used in Figure 4 are displayed in Figure 5. These psfs exhibit distinct heavy tail behavior not shown in Figure 5. The

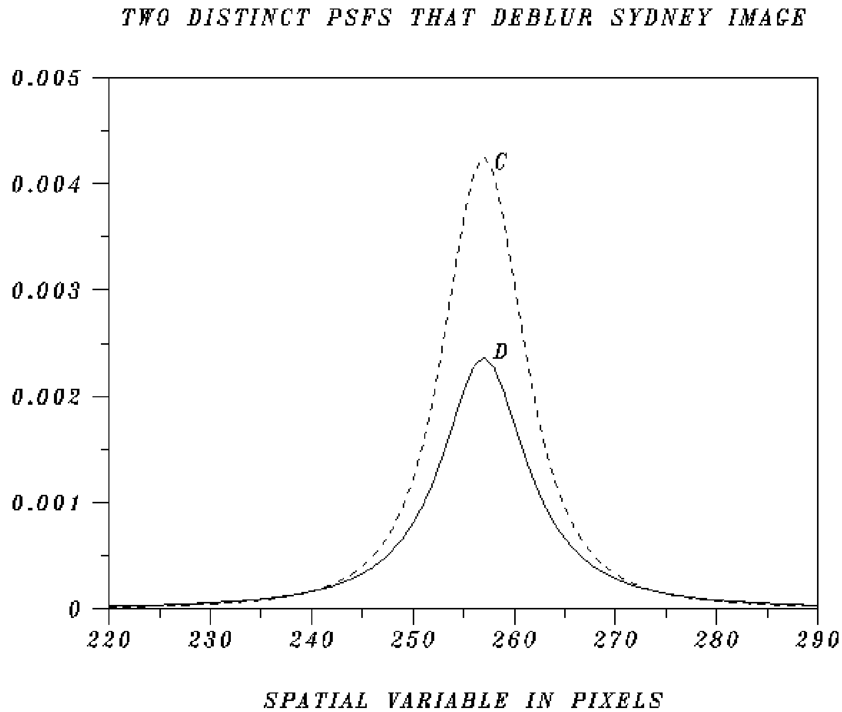

FIG. 5. *Two distinct point spread functions that deblur image (B) in Figure 4. Curves C and D are 1-D cross sections of the* 512×512 *psfs that respectively produced images (C) and (D) in Figure 4. These psfs also exhibit distinct heavy tail behavior.*

TABLE 1

Behavior in deblurred images in Figure 4.

Restoration	$\alpha, \quad \beta$	L^1 *norm*	*TV norm*
Image (C)	$\alpha = 0.075, \quad \beta = 0.500$	173	6419
Image (D)	$\alpha = 0.195, \quad \beta = 0.400$	171	7500

two restorations also have distinct L^1 and TV norms, as shown in Table 1.

Note that Figure 4(D) was obtained using a specific pair (α, β) where $\alpha > \alpha_0$, and $\beta < \beta_0$. In fact, there are infinitely many other specific pairs (α, β), capable of producing distinct, high quality reconstructions from the same blurred image $g_e(x, y)$ in Figure 4(B). These reconstructions may differ markedly from one another at individual pixels, while being correct visual representations of the object that was imaged. This is an inherent, a-priori, non-uniqueness property of the blind deconvolution problem, independently of any particular algorithm that might be used to solve that problem.

This situation is reminiscent of the multitude of distinct images that often exist for some unique astronomical objects, such as the Whirlpool Galaxy (M51), for example. In that case, these noticeably different photographic representations of the identical object are all physically meaningful and visually correct.

The non-uniqueness of good solutions to the blind deconvolution problem has not been fully explored in the literature. When a blind algorithm produces a unique solution, this may only indicate that that solution is the only one accessible to that particular algorithm. Conceivably, there may be numerous additional good solutions that remain inaccessible to the algorithm. And some of these reconstructions may exhibit features of great interest.

A basic property of the APEX method is that it generally provides several psfs that can be used to obtain useful reconstructions of a given blurred image. As in the example above, these reconstructions will differ from one another at individual pixels while being visually correct. As is well-known, a-priori knowledge about the desired solution is a necessary ingredient for solving ill-posed inverse problems. Such knowledge is expected to guide the user in his selection of the best solution, out of the multiplicity of good solutions.

7. Slow motion blind deconvolution and the APEX method. The following observations underlie the APEX method. In the basic relation

$$g(x,y) = h(x,y) \otimes f_e(x,y) + n(x,y), \tag{19}$$

we may safely assume that the noise $n(x,y)$ satisfies

$$\int_{R^2} |n(x,y)| dxdy \ll \int_{R^2} f_e(x,y) dxdy = \gamma > 0, \tag{20}$$

so that,

$$|\hat{n}^*(\xi,\eta)| \ll 1. \tag{21}$$

Consider the case where the otf is a pure Lévy density $\hat{h}(\xi,\eta) = e^{-\alpha(\xi^2+\eta^2)^\beta}$. Since $g = g_e + n$

$$\ln|\hat{g}^*(\xi,\eta)| = \ln|e^{-\alpha(\xi^2+\eta^2)^\beta}\hat{f_e}^*(\xi,\eta) + \hat{n}^*(\xi,\eta)|. \tag{22}$$

Let $\Omega = \{(\xi,\eta) \mid \xi^2+\eta^2 \leq \omega^2\}$ be a neighborhood of the origin where

$$e^{-\alpha(\xi^2+\eta^2)^\beta}|\hat{f_e}^*(\xi,\eta)| \gg |\hat{n}^*(\xi,\eta)|. \tag{23}$$

Such an Ω exists since Eq. (23) is true for $\xi = \eta = 0$ in view of Eq. (21). The radius $\omega > 0$ of Ω decreases as α, β, and n increase. However, in many applications, α, β, and $n(x,y)$ are sufficiently small that Ω extends into the high-frequency range. For $(\xi,\eta) \in \Omega$ we have

$$\ln|\hat{g}^*(\xi,\eta)| \approx -\alpha(\xi^2+\eta^2)^\beta + \ln|\hat{f_e}^*(\xi,\eta)|. \tag{24}$$

Because of the radial symmetry in the psf, it is sufficient to consider Eq. (24) along a single line through the origin in the (ξ,η) plane. Choosing the line $\eta = 0$, we have

$$\ln|\hat{g}^*(\xi,0)| \approx -\alpha|\xi|^{2\beta} + \ln|\hat{f_e}^*(\xi,0)|, \qquad |\xi| \leq \omega. \tag{25}$$

Some type of a-priori information about $f_e(x,y)$ is necessary for blind deconvolution. In Eq. (25), knowledge of $\ln|\hat{f_e}^*(\xi,0)|$ on $|\xi| \leq \omega$ would immediately yield $\alpha|\xi|^{2\beta}$ on that interval. Moreover, any other line through the origin could have been used in Eq. (24). However, $\ln|\hat{f}_e^{\,*}(\xi,0)|$ is highly oscillatory, and such detailed knowledge is unlikely in practice. Nor is it actually necessary. Much cruder knowledge, in the form of the smooth curve Γ that best approximates $\ln|\hat{f}_e^{\,*}(\xi,0)|$ in the least squares sense, turns out to be sufficient. Indeed, knowledge of the smooth curve Γ is the basis for the *BEAK method* of determining α and β from Eq. (25). See [4]. However, when Γ is not available, the APEX method must identify a useful psf from Eq. (25), using more elusive information about $\ln|\hat{f}_e^{\,*}(\xi,0)|$. To compensate for this handicap, the SECB *marching backwards in time* option in Eq. (15) is used, together with visual monitoring of the unfolding deconvolution. Accompanying diagnostic statistical information as $t \to 0$, such as the discrete norms $\parallel u^{\dagger}(t) \parallel_{L^1}$, and $\parallel u^{\dagger}(t) \parallel_{TV}$, in Eqs. (16) and (17), provide the means for readjusting initially detected psf parameters, α and β, and *enforcing conservation of total flux*. The method assumes that $f_e(x,y)$ is a recognizable object, and typically requires several interactive trials prior to locating a suitable psf. As previously noted, such trial SECB restorations are easily obtained.

7.1. Conservation of total flux. In the absence of the smooth least squares fit Γ, we replace $\ln|\hat{f}_e^{\,*}(\xi,0)|$ by a negative constant $-A$ in Eq. (25). For any $A > 0$, the approximation

$$\ln|\hat{g}^*(\xi,0)| \approx -\alpha|\xi|^{2\beta} - A, \tag{26}$$

is not valid near $\xi = 0$, since the curve $u(\xi) = -\alpha|\xi|^{2\beta} - A$, has $-A$ as its apex. Choosing a value of $A > 0$, we best fit $\ln|\hat{g}^*(\xi,0)|$ with $u(\xi) = -\alpha|\xi|^{2\beta} - A$ on the interval $|\xi| \leq \omega$, using nonlinear least squares algorithms. The resulting fit is close only for ξ away from the origin. The returned values for α and β are then used in the SECB deblurring algorithm. Different values of A return different pairs (α,β). Experience indicates that useful values of A generally lie in the interval $3 \leq A \leq 6$. Increasing the value of A decreases the curvature of $u(\xi)$ at $\xi = 0$, resulting in a larger value of β together with a smaller value of α. A value of $A > 0$ that returns $\beta > 1$ is clearly too large, as $\beta > 1$ is impossible for probability density functions [9]. Decreasing A has the opposite effect, producing lower values of β and higher values of α. As a rule, deconvolution is better behaved at lower values of β than it is when $\beta \approx 1$. A significant discovery is that *an image blurred with a pair* (α_0,β_0) *can often be successfully deblurred with an appropriate pair* (α,β), *where* $\alpha > \alpha_0$ *and* $\beta < \beta_0$. An example of this phenomenon was shown in Figure 4(D) in connection with the blurred Sydney image. An effective interactive framework for performing the above least squares fitting is the *fit* command in *DATAPLOT* [11]. This is a high-level English-syntax graphics and analysis software package developed at the National Institute of Standards and Technology. This software tool was used throughout this paper.

The following version of the APEX method has been found useful in a variety of image enhancement problems where the image $g(x,y)$ is such that $\ln|\hat{g}^*(\xi,0)|$ is generally globally monotone decreasing and convex, as shown in Figure 3(A). Choose a value of $A > 3$ in Eq. (26), so that the least squares fit develops a well-formed *cusp* at $\xi = 0$, as shown in Figure 3(B). Using the returned pair (α,β) in the SECB method, obtain a sequence $u^{\dagger}(x,y,t)$ of partial restorations as in Eq. (15), as t decreases from $t = 1$. With a good choice of A, the total flux norm, $\parallel u^{\dagger}(t) \parallel_{L^1}$, should remain constant or increase very slowly as t decreases, while the image gradient norm, $\parallel u^{\dagger}(t) \parallel_{TV}$, should increase monotonically as t decreases from $t = 1$.

Most often, the initially detected value of α turns out to be *too large*. The corresponding psf is then *too wide* in physical (x, y) space, or, equivalently, the otf is too narrow in Fourier (ξ, η) space. Theoretically, use of too wide a psf all the way to $t = 0$, implies sharpening features that may have already become infinitely sharp at some $t_\sigma > 0$. In practice, this leads to severe ringing and other undesirable artifacts at $t = 0$, indicating that continuation backwards in time has proceeded *too far*. An accompanying symptom of this ill-behaved deconvolution, is that the total flux norm $\| u^\dagger(t) \|_{L^1}$ does not remain constant, but increases appreciably as $t \to 0$. Choosing a new and larger value of A in Eq. (26), returns a smaller α, but with a larger β. A useful strategy is to locate a pair (α, β) such that $\| u^\dagger(t) \|_{L^1}$ increases slowly enough as t decreases, that its value at $t = t_\sigma = 0.5$, say, is only a very few percent more than its initial value at $t = 1$. In that case, the deconvolution is terminated at $t = t_\sigma$. To enforce total flux conservation, the resulting image at t_σ is rescaled by multiplying it by the constant $C_\sigma = \| u^\dagger(1) \|_{L^1} / \| u^\dagger(t_\sigma) \|_{L^1}$. Ideally, C_σ should be very close to unity.[1]

Marching backwards in time allows for simultaneous sampling of numerous values of α while keeping β fixed. Terminating the deconvolution at $t = t_\sigma > 0$, is equivalent to readjusting the original α while keeping the same value of β. If the pair (α, β) produces a high quality restoration at $t = t_\sigma > 0$, the pair (α^*, β), where $\alpha^* = (1 - t_\sigma)\alpha$, will produce the same quality results at $t = 0$. We therefore distinguish between the originally detected α, and the *effective* α, α^*. In general, there will be many values of A in (26) returning pairs (α, β) that produce good reconstructions at some $t_{\alpha\beta} > 0$. A large number of distinct pairs (α^*, β) can thus be found that produce useful, but distinct, results at $t = 0$. Ideally, successful APEX blind deconvolution should incorporate three elements: clear visual evidence of sharpening, accompanied by a substantial increase in TV norm, and conservation of L^1 norm.

We have been assuming $\hat{h}(\xi, \eta)$ to be a pure Lévy otf in Eq. (19). The procedure is very similar for the more general class $\mathbf{G}$ otfs in Eq. (4). Here, given prior starting values for the $\alpha_i,\ \beta_i,\ i = 1, J$, we best-fit $\ln |\hat{g}^*(\xi, 0)|$ with $-\sum_{i=1}^{J} \alpha_i |\xi|^{2\beta_i} - A,$, with suitably preselected $A > 3$. This returns J initially detected pairs (α_i, β_i). As before, by monitoring the deconvolution process and terminating it at the appropriate time $t_\sigma > 0$, we arrive at effective values $\alpha_i^* = (1 - t_\sigma)\alpha_i$, such that the J pairs (α_i^*, β_i) produce useful sharpening at $t = 0$. It should be noted that in most applications of the APEX method considered to date, including those in the present paper, high quality reconstructions were obtained using the simplest version of that method, where $J = 1$. This indicates that in many applications, a single pure Lévy stable otf can often be found that sufficiently well-approximates the system's more complex composite otf.

All point spread and optical transfer functions depicted in this paper, including those in Figure 5, are based on *effective* Lévy parameter values (α^*, β), producing optimal reconstructions at $t = 0$.

8. Applications to gray scale galaxy images. Our first example, in Figure 6(A), is a 1024×1024 8-bit gray scale image $g(x, y)$ of the spiral galaxy M101. This is adapted from a similar size color JPEG image obtained by Jacoby, Bohannan, and Hanna, Kitt Peak National Optical Astronomy Observatory, (NOAO/AURA/NSF). A plot of $\ln |\hat{g}^*(\xi, 0)|$ was shown earlier in Figure 3(A). Using $A = 3.85$, we best-fit $\ln |\hat{g}^*(\xi, 0)|$ with $-\alpha|\xi|^{2\beta} - A,$, on $|\xi| \leq 500$. The fit develops a well-formed cusp

[1] It is occasionally beneficial to allow more aggressive deblurring, with the L^1 norm increasing by as much as 10% prior to rescaling, in order to bring out important fine scale structural details.

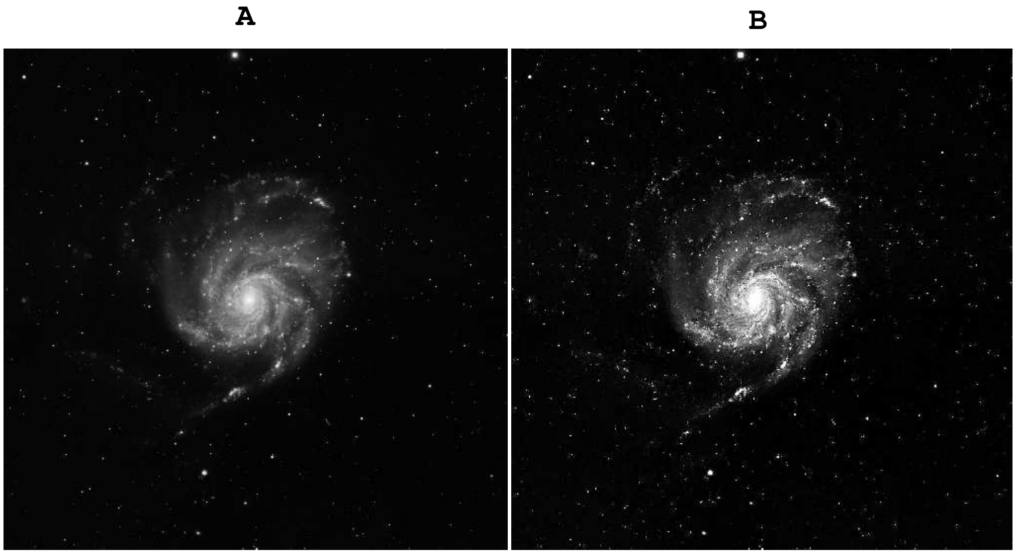

Fig. 6. *APEX blind deconvolution of M101 image. (A) Original* 1024×1024 *M101 image, obtained by Jacoby, Bohannan, and Hanna, Kitt Peak National Observatory, (NOAO/AURA/NSF). (B) APEX processed image is noticeably sharper. Both images have identical* L^1 *'total flux' norms, but TV 'gradient' norm in image (B) is three times larger than in image (A).*

at $\xi = 0$, as shown in Figure 3(B), and returns $\alpha = 0.385,\ \beta = 0.206$. The patterns illustrated in Figure 3 are typical of all the images discussed in this paper. Using these Lévy parameters in the SECB method with $s = 0.01,\ K = 1300$, we find that at first, $\| u^{\dagger}(t) \|_{L^1}$ increases slowly as t decreases, from an initial value of 12.84 at $t = 1$, to a value of 12.96 at $t = 0.65$. Thereafter, $\| u^{\dagger}(t) \|_{L^1}$ increases more rapidly. At the same time, $\| u^{\dagger}(t) \|_{TV}$ increases monotonically from 2134 at $t = 1$, to 6747 at $t = 0.65$, i.e., a threefold increase in gradient norm. Deconvolution was terminated at $t_\sigma = 0.65$, and the effective value of α is $\alpha^* = 0.135$. The APEX-processed image, shown in Figure 6(B), was rescaled so as to have the same L^1 norm as Figure 6(A).

Our second example, in Figure 7(A), is a 1024x1024 8-bit gray scale image of the spiral galaxy M51. This is adapted from a similar size color JPEG image obtained by Rector and Ramirez, Kitt Peak National Optical Astronomy Observatory, (NOAO/AURA/NSF). Here, there is very substantial documented APEX sharpening, and the deconvolved image in Figure 7(B) very visibly improves on the original. With A=5.0, least squares fitting on $|\xi| \leq 500$, returned $\alpha = 0.364, \beta = 0.218$. This was input into the SECB method with s=0.01, K=1300. Deconvolution was terminated at $t_\sigma = 0.48$, leading to an effective $\alpha^* = 0.189$. Total flux $\| u^{\dagger}(t) \|_{L^1}$ increased very slightly, from 30.58 at $t = 1$, to 30.82 at $t_\sigma = 0.48$. However, there was a corresponding *eightfold* increase in $\| u^{\dagger}(t) \|_{TV}$, from 1948 at $t = 1$, to 16516 at $t_\sigma = 0.48$. Both images in Figure 7 have identical L^1 norms.

Our next example, in Figure 8(A), is a 1024×1024 8-bit gray scale image of the spiral galaxy M74. This is adapted from a JPEG color image taken in August 2001 by the GMOS Team at the Gemini Observatory, Mauna Kea, Hawaii. With $A = 4.25$, least squares fitting of $\ln |\hat{g}^*(\xi, 0)|$ with $-\alpha |\xi|^{2\beta} - A$, on $|\xi| \leq 500$, returned $\alpha = 0.857,\ \beta = 0.157$. Here, more aggressive deblurring was permitted prior to termination. With $s = 0.01$ and $K = 500$ in the SECB method, $\| u^{\dagger}(t) \|_{L^1}$

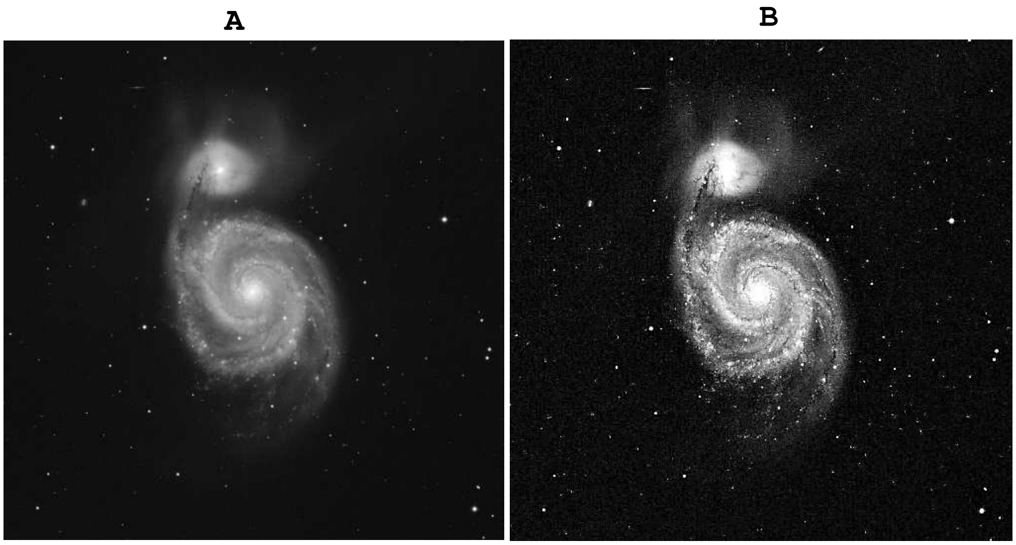

Fig. 7. *Blind deconvolution of M51 image. (A) Original* 1024×1024 *M51 image obtained by Rector and Ramirez, Kitt Peak National Observatory, (NOAO/AURA/NSF). (B) APEX processing very significantly improves original. 'Total flux'* L^1 *norms of images (A) and (B) are equal, but 'gradient' TV norm in (B) is more than eight times larger than in (A).*

increased by 7%, from 61.22 to 65.68, prior to termination at $t_\sigma = 0.65$. The effective value of α is $\alpha^* = 0.3$, and there was a corresponding fourfold increase in $\| u^\dagger(t) \|_{TV}$, from 4670 to 20173. The APEX-processed image in Figure 8(B) was rescaled so as to have the same L^1 norm as Figure 8(A).

In Figure 9, $\ln |\hat{g}^*(\xi, 0)|$ is plotted on $|\xi| \leq 500$, for the M51 and M74 images, before and after APEX processing. Evidently, APEX processing amplifies high frequency components quite significantly. This amplification is carefully orchestrated, takes place in a stable, coherent fashion, and enables recovery of the delicate fine structures and other features that are evident in Figures 7(B) and 8(B). These before and after Fourier patterns are typical of all the images shown in this paper.

9. APEX processing of color imagery. Blind deconvolution of color imagery is a subject that is still very much in its infancy. Major difficulties arise from the need to identify the distinct point spread functions associated with each color component. More serious difficulties arise from the possibility of *unbalanced* blind sharpening of individual color components. Conceivably, after a long and uncertain iterative process, the reconstituted color image may turn out to exhibit physically false colors, such as a green sky, or a purple sea. A fruitful mathematical framework wherein the blind color problem can be effectively tackled, has not yet been formulated.

One approach to color image processing traces its origin to high energy physics and string theory [18], [26], [27]. Here, a color image is viewed as a $2D$ manifold in $5D$ space, namely, $\{x, y, R(x,y), G(x,y), B(x,y)\}$, where $R,\ G,\ B$ are the red, green, and blue components of the color image $g(x,y)$. The so-called Polyakov functional is then defined on this manifold, and gradient descent minimization of this functional is implemented. This leads to the *Beltrami flow* equations, a coupled system of evolutionary nonlinear partial differential equations for the three time-dependent images $R(x,y,t),\ G(x,y,t),\ B(x,y,t)$. That system is then solved forward in time numeri-

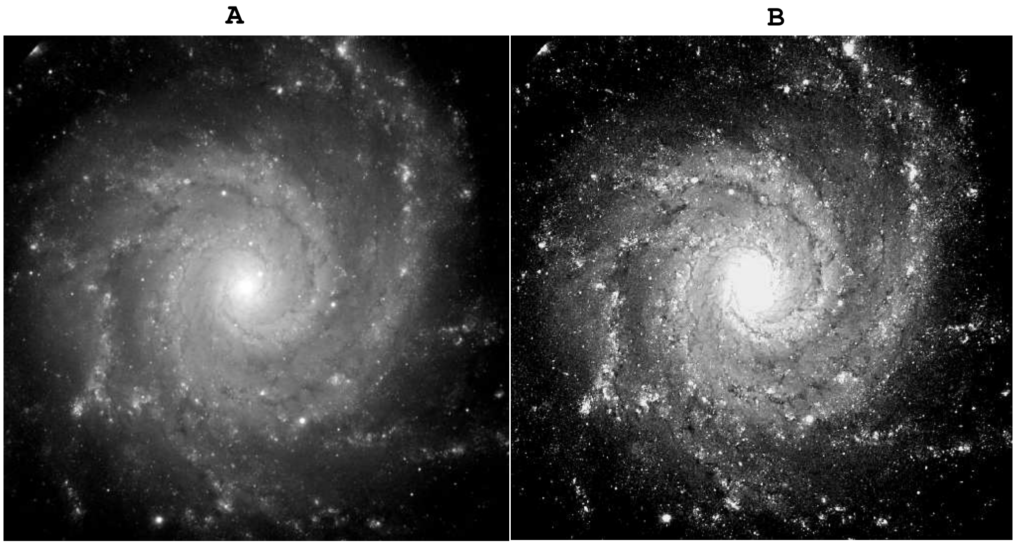

FIG. 8. *Blind deconvolution of M74 image. (A) Original* 1024×1024 *M74 image obtained by GMOS Team at Gemini Observatory, Mauna Kea, Hawaii. (B) APEX processing significantly improves original. 'Total flux'* L^1 *norms in images (A) and (B) are equal, but 'gradient' TV norm in (B) is four times larger than in (A).*

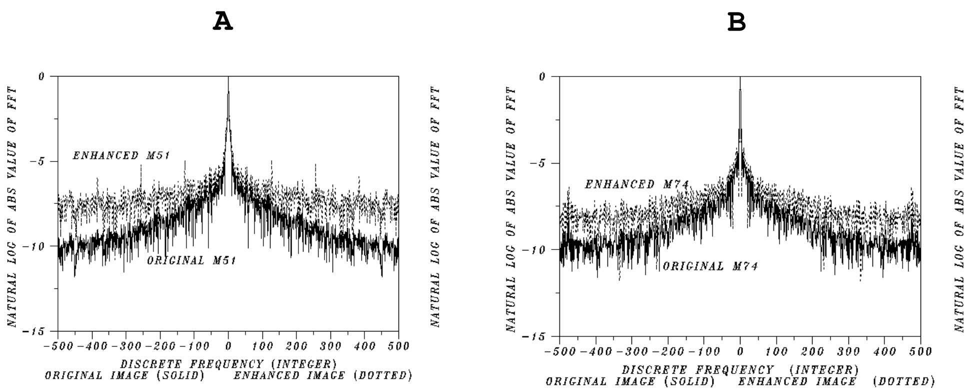

FIG. 9. *APEX processing leads to significant change in high frequency Fourier behavior. (A) Before and after for M51 image. (B) For M74 image.*

cally, until a steady-state is reached. This formalism has been applied successfully to color image denoising. With considerable skill, such an approach might possibly be elaborated into a blind deconvolution procedure. However, the computational effort required to process large size imagery would be challenging.

A remarkable property of the APEX method is the ease with which it can be applied to color imagery, and the plausibility of the ensuing results. Clearly, the ability to try numerous parameter values in quasi real-time is of vital significance. Indeed, efficient exploration in parameter space is often the key to the successful solution of ill-posed inverse problems.

The most natural way to use the APEX method is to first decompose the blurred color image into its three RGB components, apply the method to each component in turn, and then reconstitute the deblurred image. For each RGB component, visual monitoring of the partial deconvolution $u^\dagger(x,y,t)$ in Eq. (15) as $t \to 0$, is accompanied by the calculated diagnostic quantities $\| u^\dagger(t) \|_{L^1}$ and $\| u^\dagger(t) \|_{TV}$. As in the case of gray scale imagery discussed above, total flux conservation in each RGB component is enforced by terminating deconvolution at some appropriate time $t_\sigma > 0$, and rescaling the image by multiplication by the constant $C_\sigma = \| u^\dagger(1) \|_{L^1} / \| u^\dagger(t_\sigma) \|_{L^1}$. In this way, individual Lévy pairs (α^*, β) are detected for each RGB component, often leading to distinct otfs for each color. This methodology has also been found to maintain the balance of colors in all of the many examples to which it has been applied. We shall now demonstrate this on several color images, including some spectacular Hubble Space Telescope images.

Our first color image, in Figure 10(A), is an Ektachrome 1024×727 tiff image of the Southern Pinwheel galaxy M83. This was downsized from an original 3500×2485 tiff image taken by Bill Schoening at Kitt Peak National Optical Astronomy Observatory, (NOAO/AURA/NSF). After decomposition into RGB components, APEX least squares fitting on $|\xi| \leq 500$, with $A = 3.85$, was applied to each component. The returned values for α and β were then input into the SECB method with $s = 0.01$, $K = 1300$. For the red component, $\alpha = 0.356$, $\beta = 0.195$, and $\| u^\dagger(t) \|_{L^1}$ increased by about 2%, from 15.02 to 15.36, prior to termination at $t_\sigma = 0.65$. The effective α in this case is $\alpha^* = 0.124$. There was a corresponding threefold increase in $\| u^\dagger(t) \|_{TV}$, from 2541 to 7698. For the green component, $\alpha = 0.506$, $\beta = 0.171$, and the L^1 norm increased by 5%, from 23.76 to 24.99, prior to termination at $t_\sigma = 0.65$. Here, $\alpha^* = 0.177$. There was again a threefold increase in TV norm, from 4393 to 14613. For the blue image, $\alpha = 0.571$, $\beta = 0.161$, and $\| u^\dagger(t) \|_{L^1}$ increased by 6.5%, from 30.60 to 32.59, prior to termination at $t_\sigma = 0.65$. This gives $\alpha^* = 0.2$. Once again, there was a threefold increase in $\| u^\dagger(t) \|_{TV}$, from 3606 to 11778.

In this example, the green image otf almost coincides with the blue image otf, and both lie below the red image otf. Thus, the APEX method perceived the red component to be less blurred than the other two components, and it processed the image accordingly. All three components were rescaled to preserve L^1 norms, prior to reconstitution into Figure 10(B).

The next example is a Hubble Space Telescope image of NGC2207, involving two merging galaxies. That image forms part of the Hubble Heritage Gallery. The original full resolution 2907×1486 tiff image was obtained by NASA, ESA, and the Hubble Heritage Team (STSci/AURA), using the Wide Field and Planetary Camera 2, (WFPC2). This was stepped down to the 1024×523 shown in Figure 11(A). We used $A = 4.75$ with $s = 0.01$, $K = 1300$ in the SECB method, and terminated the process at $t_\sigma = 0.65$ in each of the three components. Here, APEX perceived the red component to be more blurred than the other two components. For the red image, $\alpha^* = 0.111$, $\beta = 0.203$, and $\| u^\dagger(t) \|_{L^1}$ increased by 10.25%, from 19.11 to 21.06, while $\| u^\dagger(t) \|_{TV}$ increased from 3862 to 11182, a factor of 2.9. For the green image, $\alpha^* = 0.088$, $\beta = 0.217$, $\| u^\dagger(t) \|_{L^1}$ increased from 17.71 to 18.82, (6.8%), while $\| u^\dagger(t) \|_{TV}$ increased by a factor of 2.8, from 3937 to 11019. The blue image was perceived to be the least blurred. Here, $\alpha^* = 0.052$, $\beta = 0.247$, $\| u^\dagger(t) \|_{L^1}$ increased by 8.9%, from 14.67 to 15.97, while $\| u^\dagger(t) \|_{TV}$ increased by a factor of 2.4, from 7783 to 17726. All three RGB components were rescaled to prserve L^1 'total flux' norms, prior to reconstitution into Figure 11(B).

Our third example is again a Hubble Heritage Gallery image, featuring the re-

A

B

FIG. 10. *APEX processing significantly sharpens Southern Pinwheel M83 Ektachrome image. Original (A) was obtained by Bill Schoening, Kitt Peak National Observatory, (NOAO/AURA/NSF). Both images have equal* L^1 *'total flux' norms in each RGB component, while component TV 'gradient' norms in enhanced image (B) are three times larger than in (A).*

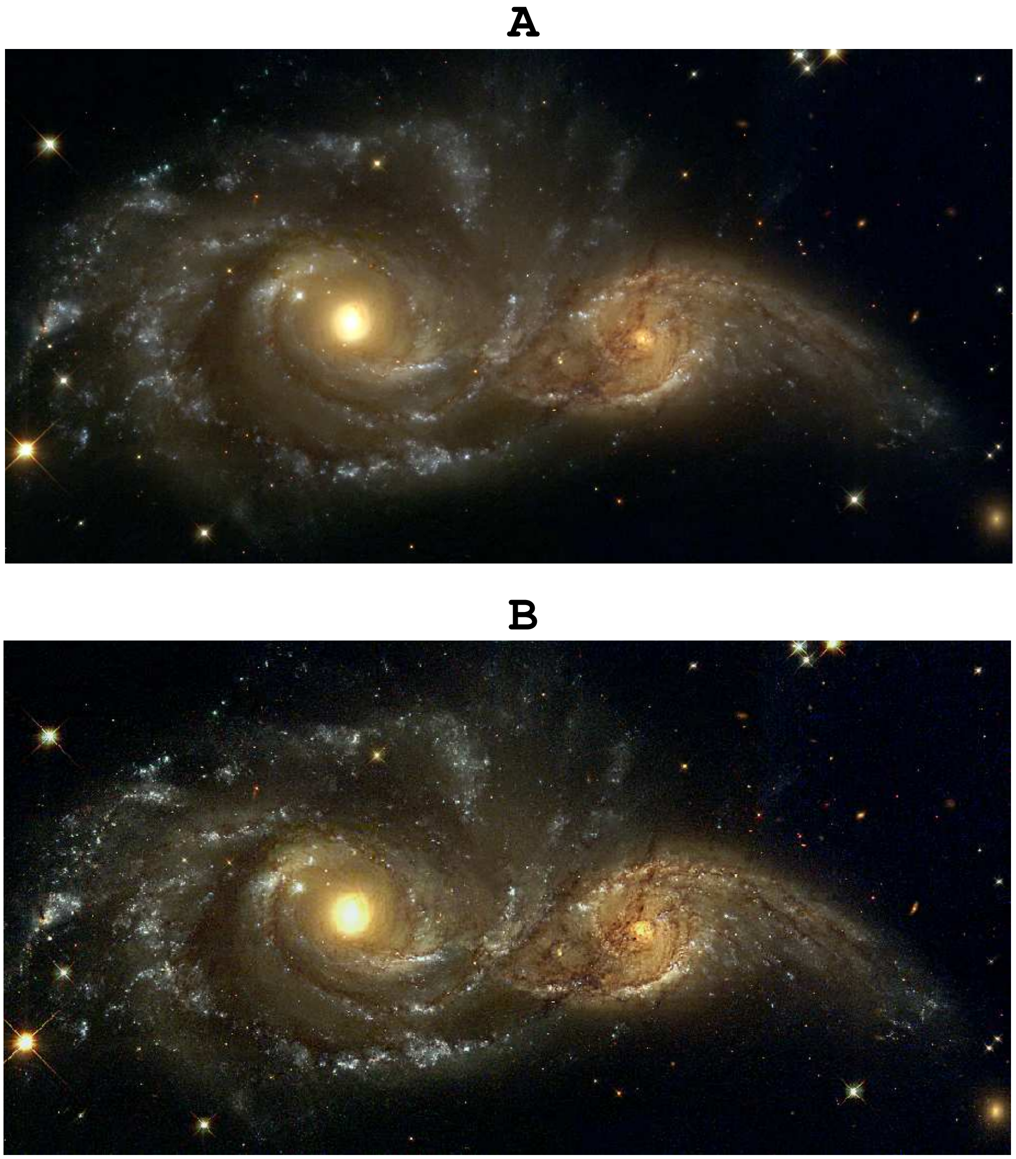

Fig. 11. *APEX processing enhances Hubble Space Telescope image of NGC2207 involving two merging galaxies. Original (A) was obtained by NASA, ESA, and the Hubble Heritage Team (STSci/AURA). Both images have equal L^1 'total flux' norms in each RGB component, while component TV 'gradient' norms in enhanced image (B) are almost three times larger than in (A).*

flection nebula in Orion, NGC 1999. The original 750×750 tiff image was obtained by NASA and the Hubble Heritage Team (STSci/AURA), using the WFPC2 camera. Here, this was stepped down to the 512×512 image shown in Figure 12(A). With $A = 5.5$ and $s = 0.01$, $K = 1300$ in SECB, deconvolution was unusually well-behaved and *uniform*. For each RGB component, $\| u^{\dagger}(t) \|_{L^1}$ was very nearly conserved prior to termination at $t_{\sigma} = 0.6$. This norm was near 97 for the blue image, and near 67 for the red and green images. Moreover, detected Lévy pairs for each component were

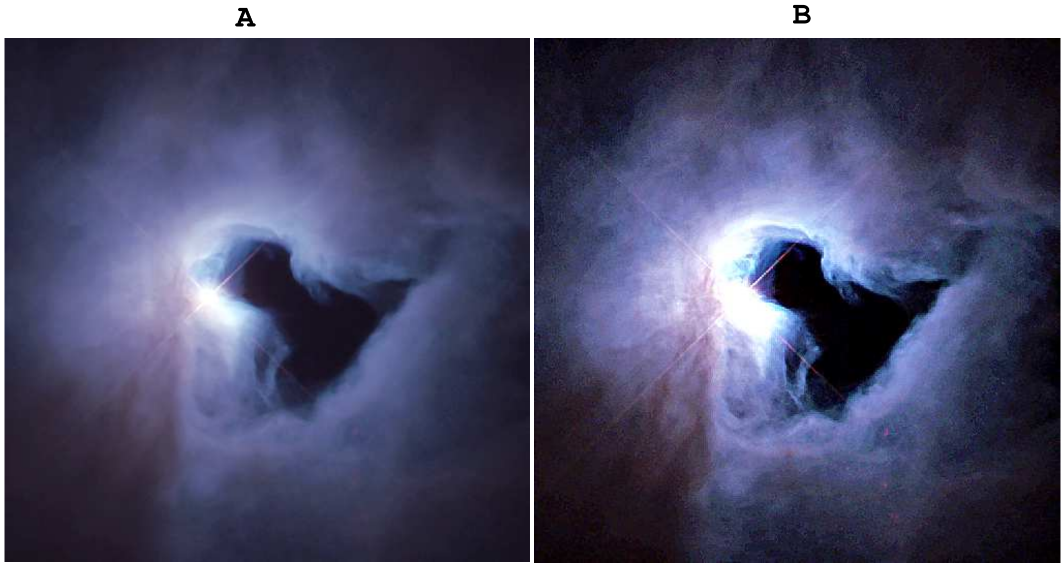

Fig. 12. *APEX blind deconvolution enhances Hubble Space Telescope image of Orion Reflection Nebula, NGC 1999. Original (A) was obtained by NASA and the Hubble Heritage Team (STSci/AURA). Both images have equal L^1 'total flux' norms in each RGB component, while component TV 'gradient' norms in enhanced image (B) are 5.6 times larger than in (A).*

all very nearly equal to $\alpha^* = 0.3,\ \beta = 0.17$, and all three otfs coincided in this case. Again, for each RGB component, $\| u^\dagger(t) \|_{TV}$ increased by the same factor of 5.6, from 1498 to 8539 for red, from 1450 to 8166 for green, and from 2291 to 12890 for blue.

As was the case with gray scale galaxy images, striking improvements in visual quality in Figures 10(B), 11(B), and 12(B), appear to correlate well with substantial increases in TV norms.

9.1. Advanced Camera for Surveys (ACS) imagery. The WFPC2 is Hubble's main camera and workhorse instrument. Our final two examples feature images taken with the Advanced Camera for Surveys (ACS). That instrument outperforms all previous cameras aboard the Hubble Space Telescope. To celebrate Hubble's fifteenth birthday on April 25 2005, NASA released the sharpest-ever color image of the Whirlpool Galaxy M51. That image was recorded with the ACS Camera by NASA, ESA, S. Beckwith (STScI), and the Hubble Heritage Team (STScI/AURA). The original full resolution 7965×11477 tiff image was stepped down to the 710×1024 tiff image shown in Figure 13(A). After decomposing that image into RGB components, APEX processing using $A = 5.25$ was applied to each component in turn, with $s = 0.01,\ K = 1300$ in the SECB method. All three components behaved very similarly, and deconvolution was terminated at $t_\sigma = 0.65$ in all three cases. For the red component, $\alpha^* = 0.175,\ \beta = 0.173$, and $\| u^\dagger(t) \|_{L^1}$ increased by 5.3% prior to termination, from 42.46 to 42.72. However, $\| u^\dagger(t) \|_{TV}$ increased by a factor of 3.7, from 5170 to 19247. For the green component $\alpha^* = 0.177,\ \beta = 0.171$, and the L^1 norm increased from 41.63 to 44.05, a 5.8% increase. The TV norm increased from 4361 to 17801, a fourfold increase. For the blue component, $\alpha^* = 0.160,\ \beta = 0.186$, and the L^1 norm increased from 41.11 to 43.28, a 5.3% increase. There was again

A B

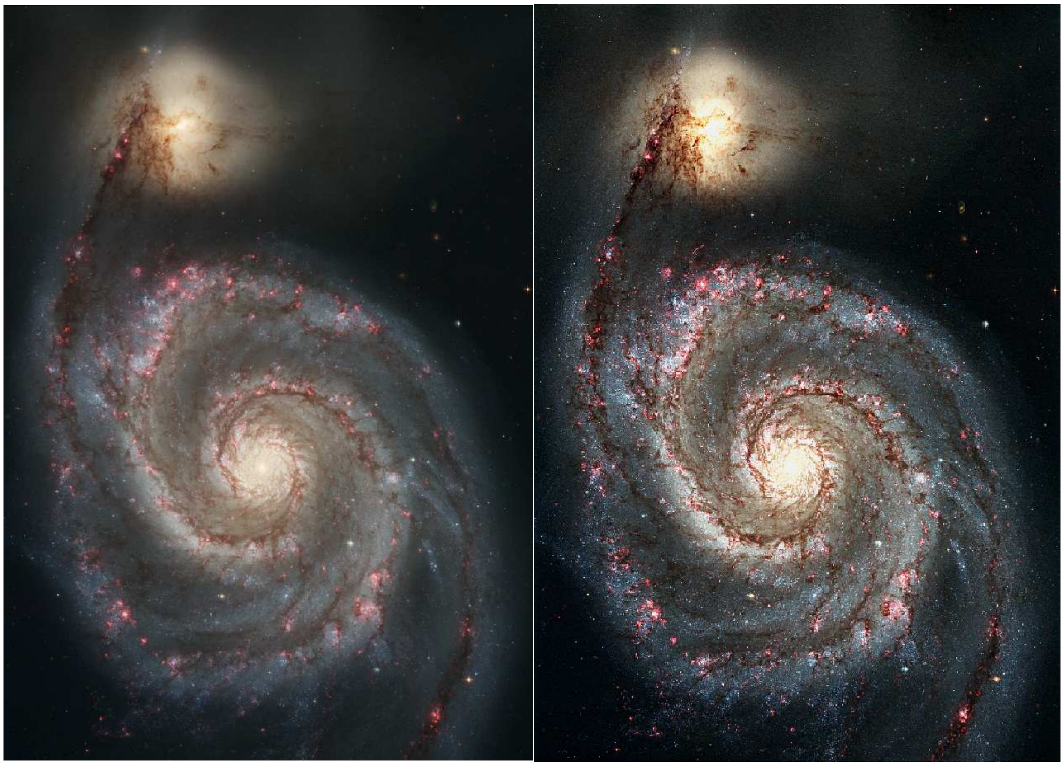

Fig. 13. *APEX processing significantly sharpens 15th anniversary Hubble Space Telescope Whirlpool galaxy image, released on April 25 2005. Original image recorded with ACS Camera by NASA, ESA, S. Beckwith (STScI), and Hubble Heritage Team (STScI/AURA). Both images have equal L^1 'total flux' norms in each RGB component, while component TV 'gradient' norms in enhanced image (B) are four times larger than in (A).*

a fourfold increase in the TV norm, from 4805 to 19839. All three component otfs coincided in this case. Individual RGB components were rescaled so as to preserve L^1 norms, prior to reconstitution as the APEX image shown in Figure 13(B).

Our last example involves an image of the Tadpole galaxy UGC10214, said to contain a "Whitman's Sampler" of galaxies that stretch back to the beginning of time. The full resolution 3806×4160 tiff image was taken with the ACS Camera by NASA, STScI, ESA, and the ACS Science Team. This was stepped down to the 937×1024 tiff image shown in Figure 14(A). After decomposing that image into RGB components, APEX processing using $A = 5.25$ was applied to each component in turn, with $s = 0.01$, $K = 1300$ in the SECB method. Deconvolution was uniformly well-behaved, and was terminated at $t_\sigma = 0.675$ in all three components. For the red component, $\alpha^* = 0.066$, $\beta = 0.242$, and $\| u^\dagger(t) \|_{L^1}$ increased by 2.2% prior to termination, from 23.54 to 24.05. At the same time, there was a threefold increase in $\| u^\dagger(t) \|_{TV}$, from 6085 to 18606. For the green component $\alpha^* = 0.068$, $\beta = 0.234$, and $\| u^\dagger(t) \|_{L^1}$ increased by 3%, from 23.025 to 23.72. Again, there was a near threefold increase in $\| u^\dagger(t) \|_{TV}$, from 6970 to 19645. For the blue component, $\alpha^* = 0.103$, $\beta = 0.201$, the L^1 norm increased by 3.2%, from 25.25 to 26.07, while the TV norm increased threefold, from 7731 to 22756. Again, all three component

A

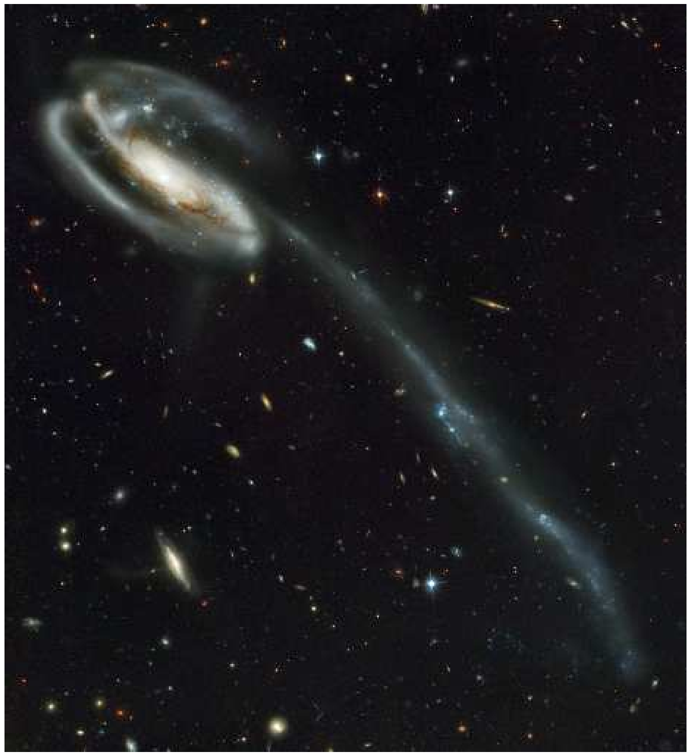

B

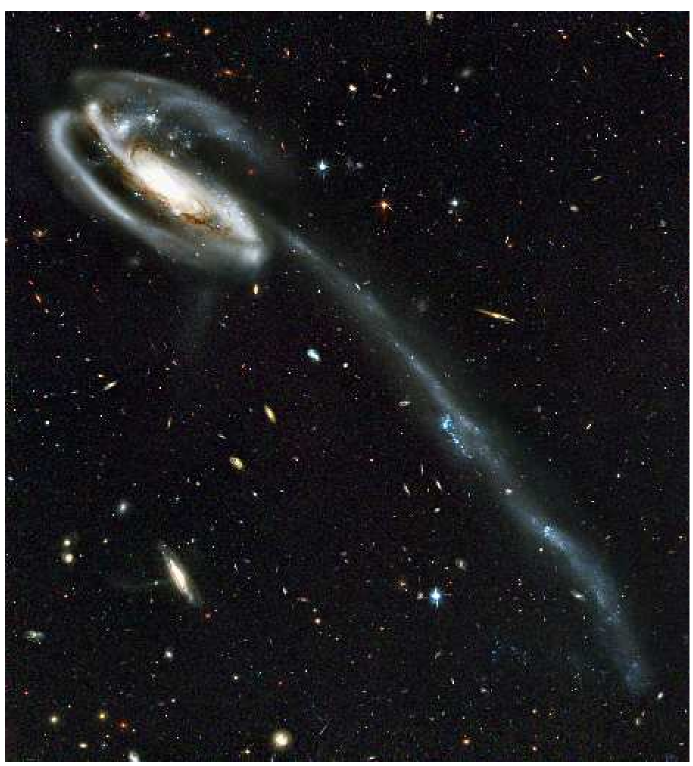

-

FIG. 14. *APEX processing enhances Hubble Space Telescope Tadpole galaxy image. Original ACS image taken by NASA, STScI, ESA, and the ACS Science Team. Both images have equal L^1 'total flux' norms in each RGB component, while component TV 'gradient' norms in enhanced image (B) are three times larger than in (A).*

A

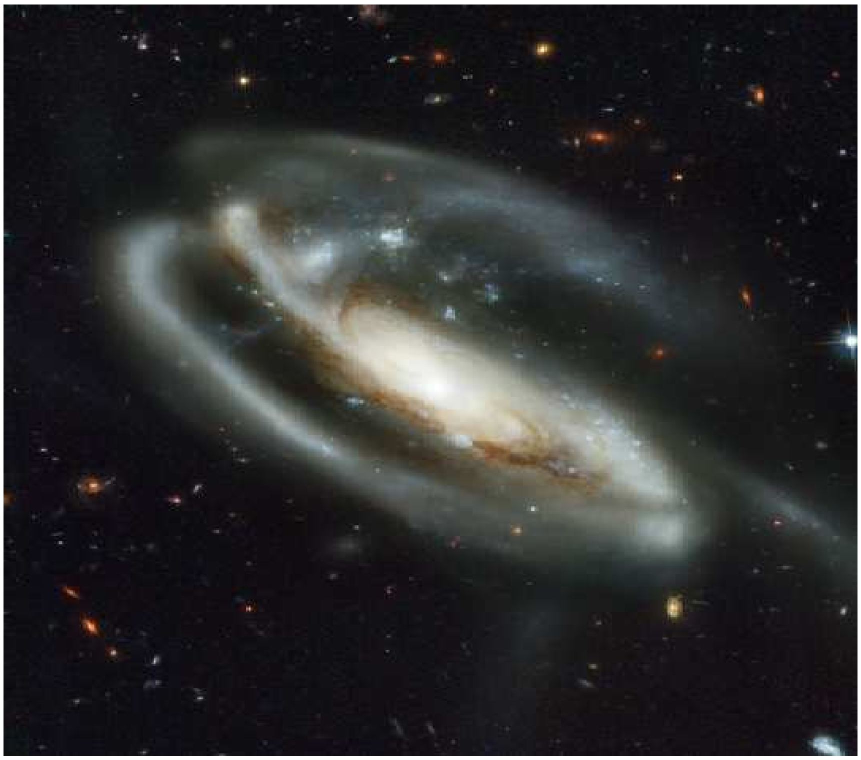

B

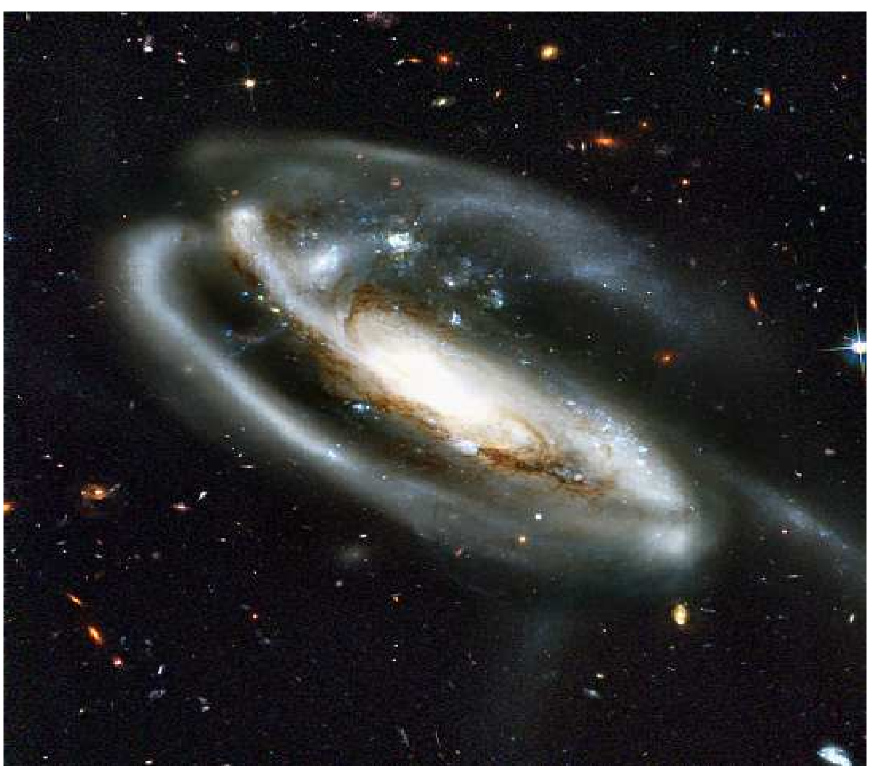

FIG. 15. *Extent of sharpening in APEX processed image becomes more evident when zooming on selected parts of images in Figure 14. Foreground objects as well as background galaxies are brought into sharper focus in Figure 15(B).*

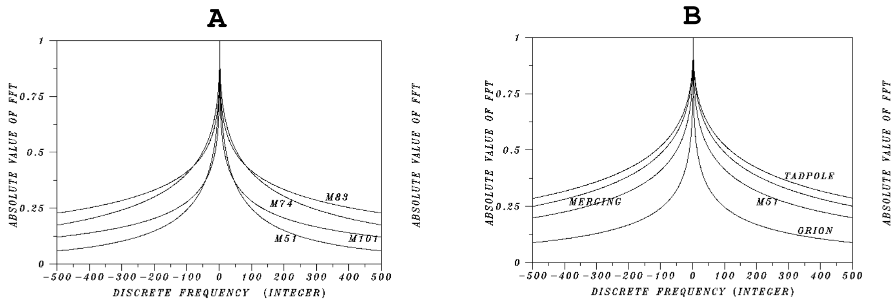

FIG. 16. *1D cross sections of optical transfer functions that deblurred images discussed in sections 8 and 9. (A) Non-Hubble otfs. (B) Hubble otfs.*

TABLE 2

Summary of APEX experiments in sections 8 and 9.

Image	*Size*	*A*	t_σ	α^*	β	$\times\, TV$
M101	1024×1024	3.85	0.65	0.135	0.206	$\times$ 3
M51 (KP)	1024×1024	5.00	0.48	0.189	0.218	$\times$ 8
M74	1024×1024	4.25	0.65	0.300	0.157	$\times$ 4
M83	1024×727	3.85	0.65	0.200	0.161	$\times$ 3
Merging	1024×523	4.75	0.65	0.111	0.203	$\times$ 3
Orion	512×512	5.50	0.60	0.300	0.168	$\times$ 6
M51 (HST)	710×1024	5.25	0.65	0.177	0.171	$\times$ 4
Tadpole	937×1024	5.25	0.65	0.068	0.234	$\times$ 3

otfs coincided. Individual RGB components were rescaled so as to preserve L^1 norms, prior to reconstitution as the APEX image shown in Figure 14(B).

Zooming on selected parts of the images in Figure 14 provides a useful comparison, as shown in Figure 15. The extent of sharpening in the APEX processed image 15(B) becomes clearly evident as foreground objects, as well as background galaxies, are brought into sharper focus.

The ability of the APEX method to enhance ACS images is remarkable and unanticipated. Figure 16 shows 1D cross-sectional plots of the optical transfer functions that were detected and used to process all of the images discussed in sections 8 and 9. Non-Hubble otfs are shown in Figure 16(A) and Hubble otfs in Figure 16(B). For color images, the narrowest otf is shown, corresponding to the blurriest RGB component. These otfs plots are based on *effective* values (α^*, β), that produce high quality SECB reconstructions at $t = 0$. These are the values shown in Table 2, which summarizes the results of the APEX experiments described in sections 8 and 9. The last column in Table 2 indicates the multiplying factors for the resulting TV norm increases.

REFERENCES

[1] H. M. Adorf, *Hubble Space Telescope image restoration in its fourth year*, Inverse Problems, 11 (1995) pp. 639-653.

[2] O. Barndorff-Nielsen, T. Mikosch and S. Resnick Eds., *Lévy Processes–Theory and Applications*, Birkhauser, Boston, 2001.

[3] A. S. Carasso, *Linear and nonlinear image deblurring: a documented study*, SIAM J. Numer. Anal., 36 (1999), pp. 1659–1689.

[4] A. S. Carasso, *Direct blind deconvolution*, SIAM J. Appl. Math., 61 (2001), pp. 1980–2007.

[5] A. S. Carasso, *The APEX method in image sharpening and the use of low exponent Lévy stable laws*, SIAM J. Appl. Math., 63 (2002), pp. 593–618.

[6] A. S. Carasso, D. S. Bright, and A. E. Vladár, *The APEX method and real-time blind deconvolution of scanning electron microscope imagery*, Optical Engineering, 41 (2002), pp. 2499-2514.

[7] A. S. Carasso, *Singular integrals, image smoothness, and the recovery of texture in image deblurring*, SIAM J. Appl. Math., 64 (2004), pp. 1749–1774.

[8] T. Csörgo, S. Hegyi, and W. A. Zajc, *Bose-Einstein correlations for Lévy stable source distributions*, Eur. Phys. J. C, 36 (2004), pp. 67-78.

[9] W. Feller, *An Introduction to Probability Theory and its Applications*, Vol. 2, Second ed., Wiley, New York, 1971.

[10] D. A. Fish, A. M. Brinicombe, and E. R. Pike, *Blind deconvolution by means of the Richardson-Lucy algorithm*, J. Opt. Soc. Am. A, 12 (1995), pp. 58-65.

[11] A. Heckert and J. J. Filliben, *DATAPLOT Reference Manual*, available on World Wide Web at http://www.itl.nist.gov/div898/software/dataplot/document.htm

[12] R. E. Hufnagel and N. R. Stanley, *Modulation transfer function associated with image transmission through turbulent media,* J. Opt. Soc. Am., 54 (1964), pp. 52–61.

[13] S. M. Jefferies and J. C. Christou *Restoration of astronomical images by iterative blind deconvolution*, Astrophysical Journal, 415 (1993), pp. 862-874.

[14] C. B. Johnson, *Classification of electron-optical device modulation transfer function*, Advances in Electronics and Electron Physics, Vol. 33B, (1972), pp. 579–584.

[15] C. B. Johnson, *MTFs: a simplified approach*, Electro-Optical Systems Design, 4, November 1972, pp. 22–26.

[16] C. B. Johnson, *Circular aperture diffraction limited MTF: approximate expressions*, Applied Optics, 11 (1972), pp. 1875–1876.

[17] C. B. Johnson, *MTF parameters for all photographic films listed in Kodak pamphlet P-49*, Applied Optics, 15 (1976), p. 1130.

[18] R. Kimmel, N. Sochen, and R. Malladi, *From high energy physics to low level vision*, Report LBNL 39243, (1996), Lawrence Berkeley National Laboratory, UC Berkeley, CA 94720.

[19] M. G. Löfdahl, Multi-frame blind deconvolution with linear equality constraints, SPIE Proceedings, 4792 (2002).

[20] J. P. Nolan, *Numerical calculations of stable densities and distribution functions*, Stochastic Models, 13, (1997), pp. 759-774.

[21] W. K. Pratt, *Digital Image Processing*, Second ed., Wiley, New York 1991.

[22] G. Samorodnitsky and M. S. Taqqu, *Stable Non-Gaussian Random Processes: Stochastic Models with Infinite Variance*, Chapman and Hall, New York, 1994.

[23] T. J. Schulz, *Multiframe blind deconvolution of astronomical images*, J. Opt. Soc. Am. A, 10 (1993), pp. 1064-1073.

[24] T. J. Schulz, B. E. Stribling, and J. J. Miller, *Multiframe blind deconvolution with real data: imagery of the Hubble Space Telescope*, Optics Express, 1 (1997), pp. 355-362.

[25] M. F. Shlesinger, G. M. Zaslavsky and U. Frisch Eds., *Lévy Flights and Related Topics in Physics*, Lecture Notes in Physics # 450, Springer-Verlag, New York, 1995.

[26] N. Sochen and Y. Y. Zeevi, *Representation of colored images by manifolds embedded in higher dimensional non-Euclidean space*, in Proc. IEEE 1998 International Conference on Image Processing, Vol. 1, pp. 166-170, Chicago, IL 1998.

[27] N. Sochen, R. Kimmel and R. Malladi, *A general framework for low level vision*, IEEE Trans. Image Processing, 7 (1998), pp. 310-318.

[28] C. Tsallis, S. V. Levy, A. M. Souza, and R. Maynard, *Statistical-mechanical foundation of the ubiquity of Lévy distributions in nature*, Phys. Rev. Letters, 75 (1995), pp. 3589-3593.

[29] E. Thiébaut and J. M. Conan, *Strict a-priori constraints for maximum likelihood blind deconvolution*, J. Opt. Soc. Am. A, 12 (1995), pp. 485-492.

[30] C. G. Toner, S. M. Jefferies, and T. L. Duvall, Jr, *Restoration of long-exposure full-disk solar intensity images*, Astrophysical Journal, 478 (1997), pp. 817-827.

[31] R. WEBER, *The ground-based electro-optical detection of deep-space satellites*, SPIE Proceedings, 143 (1978), pp. 59–69.

[32] W. A. WOYCZYŃSKI, *Lévy processes in the physical sciences*, in *Lévy Processes–Theory and Applications*, O. Barndorff-Nielsen, T. Mikosch and S. Resnick Eds., Birkhauser, Boston 2001.